J Sol-Gel Sci Technol (2015) 76:50–57
DOI 10.1007/s10971-015-3749-6

ORIGINAL PAPER

Enhanced photocatalytic performance of Ag-decorated $BiFeO_3$ in visible light region

Huidan Lu[1,2] · Zhenyu Du[1] · Jixiang Wang[1] · Yongping Liu[1,2]

Received: 24 September 2014 / Accepted: 18 May 2015 / Published online: 28 May 2015

Abstract In this paper, a novel photocatalyst, made up of $Ag/BiFeO_3$ nanocomposites activated by visible light, was successfully synthesized using a sol–gel process, followed by a chemical reduction method. The as-prepared $BiFeO_3$ particles and $Ag/BiFeO_3$ nanocomposites were characterized by X-ray diffraction, transmission electron microscopy, scanning electron microscopy and diffuse reflectance spectroscopy. The results showed that the metal Ag nanoparticles with diameter of 20–50 nm are anchored on the surface of $BiFeO_3$. Meanwhile, the photocatalytic experiments demonstrated that the $Ag/BiFeO_3$ composites had excellent photocatalytic activity for the decomposition of methyl orange in visible light, which far exceeded that of the pure $BiFeO_3$. These results revealed Ag loading could significantly improve the photocatalytic property of $BiFeO_3$. Recycle experiments showed the nanocomposites had an excellent recoverability, suggesting stable photoactivity. Finally, we discuss the photocatalytic mechanism of nanocomposites. The enhanced photoactivity of Ag-decorated $BiFeO_3$ photocatalyst is most likely attributed to the electronic effect of Ag nanoparticles including surface plasmon resonance.

Graphical Abstract

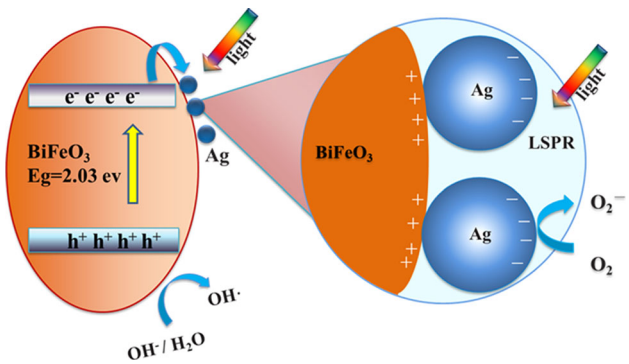

Keywords $BiFeO_3$ · Ag decoration · Nanocomposites · Photocatalysis · Surface plasmon resonance effect

1 Introduction

Among all the perovskite materials with ABO_3 structure studied so far, $BiFeO_3$ (BFO) shows ferroelectric properties with a high Curie temperature ($T_C \sim 830$ °C) and G-type antiferromagnetic properties below the Néel temperature ($T_N \sim 370$ °C) [1–4]. Therefore, it has been widely used in magnetic and ferroelectric devices [5]. Apart from ferroelectric properties, $BiFeO_3$ is one of the materials with the largest known electric polarizations and has a small (≈ 2 eV) band gap for which it is likely applied in conducting domain walls, catalyst and fuel and/or solar cells [6–11]. Recently, it has also been demonstrated that nano-BFO exhibits photocatalytic activities under visible light irradiation for water splitting and degradation of organic

✉ Yongping Liu
liuyp624@163.com

[1] College of Chemistry and Bioengineering, Guilin University of Technology, Guilin 541004, People's Republic of China

[2] Guangxi Key Laboratory of Electrochemical and Magnetochemical Function Materials, Guilin University of Technology, Guilin 541004, People's Republic of China

pollutants because of its narrow band gap and excellent chemical stability [12–15]. Li et al. [12] successfully synthesized $BiFeO_3$ microcrystals with various shapes and sizes, suggesting that photocatalytic activity of microcubes was better than that of microspheres for the degradation of Congo red under visible light irradiation. Wang et al. [13] also demonstrated that the $BiFeO_3$ nanoparticles with an average diameter of 35 nm provided the better photocatalytic performance than the bulk in the degradation of rhodamine B. Otherwise, Fei et al. [16] studied {111} dominant pills and rods of $BiFeO_3$ with a significant enhanced visible light response, and their results showed that $BiFeO_3$ with the designed structures could have a better performance in photocatalytic applications.

Although nanocrystallization and controlling of topography can improve properties of BFO over bulk materials, the low photocatalytic activity of BFO hinders its commercialization in photocatalytic field for the degradation of organic pollution. Therefore, an important task is to improve the photocatalytic activity of BFO for practical use. In fact, doping of BFO with a foreign atom at either A or B site of the ABO3 lattice has been proven to be a valuable route to enhancing its properties [17–19]. Guo et al. [20] demonstrated substitution of Bi^{3+} with Gd resulted in remarkable improvement of the photocatalytic activity of BFO under visible light. Design and construction of heterojunction is another useful method for increasing photocatalytic efficiency [21, 22]. The heterojunction usually is formed between two different semiconductors, whose inner electric field can provide a driving force for the separation of photogenerated charge carriers. Heterojunction, constructed by coating wide-gap semiconductor on narrow-gap semiconductor, can utilize photoresponse ability of both semiconductors. Otherwise, the heterojunction constructed by metal and semiconductor is called Schottky junction. On the ideal condition, because the Fermi level of metal is lower than semiconductor, photogenerated electrons migrate to the surface of metal when irradiated, which inhibit the recombination of electron and hole and promote photocatalytic efficiency. Li's group fabricated $BiFeO_3$–graphene nanohybrids through a facile hydrothermal treatments, which had a significant enhanced performance in the visible light photocatalytic activity [23]. Sakar et al. synthesized the pure BFO and BFO/γ-Fe_2O_3 nanocomposite by auto-ignition technique and examined the visible light-driven photocatalytic activity of both. As a result, the pure BFO showed a moderate photocatalytic activity, while BFO/γ-Fe_2O_3 nanocomposite exhibited enhanced activity by degrading methyl orange dye [24]. But $BiFeO_3$-based Schottky junction has rarely been reported.

In this work, we synthesized Ag/$BiFeO_3$ nanohybrids by sol–gel method followed by a chemical reduction process. UV–Vis diffuse reflectance spectroscopy was employed to study the optical properties of Ag/$BiFeO_3$. Their phase structures and morphologies were characterized by X-ray diffraction (XRD), scanning electron microscopy (SEM) and transmission electron microscopy (TEM). Furthermore, the visible light photocatalytic behaviors of the as-produced Ag/$BiFeO_3$ composites were explored by the degradation of methyl orange (MO) in aqueous solution under visible light irradiation. Due to the surface modification of $BiFeO_3$ by Ag nanoparticles (Ag NPs), the absorption and photocatalytic performance of the as-prepared photocatalyst Ag/$BiFeO_3$ in the visible region was greatly enhanced, which was attributed to surface plasmon resonance effect.

2 Experimental

2.1 Reagents

Ferric nitrate ($Fe(NO_3)_3{\cdot}9H_2O$) and bismuth nitrate ($Bi(NO_3)_3{\cdot}5H_2O$) were purchased from Sigma-Aldrich, silver nitric ($AgNO_3$) and methyl orange (MO) were obtained from Shanghai Reagents Company (Shanghai, China), and citric acid was obtained from Tianjin Chemical (Tianjin, China). Other reagents were all from commercial sources with analytical purity and used as received. All stock solutions were prepared daily with deionized water treated with a water purification system (Simplicity 185, Millipore Corp., Billerica, MA).

2.2 Preparation of $BiFeO_3$ nanoparticles and nano-Ag/$BiFeO_3$

A preciously reported sol–gel process was modified to prepare $BiFeO_3$ nanoparticles [25]. Simply, $Fe(NO_3)_3{\cdot}9H_2O$ (0.01 mol) and $Bi(NO_3)_3{\cdot}5H_2O$ (0.01 mol) were dissolved in acetic acid (20 mL), and a yellowy solution was obtained. Then, citric acid of 10 g was added into the solution under magnetic stirring as a complexant. The mixture was vigorously stirred for 1 h at 50 °C to form the sol, which was then kept at 150 °C for 2–3 h to obtain dry gel. Finally, the dry gel was calcined at 550 °C for 3 h in a muffle furnace.

Ag/$BiFeO_3$ nanocomposites were prepared by chemical reduction method [26]. PVP was used as reductant for the preparation of Ag/$BiFeO_3$ nanocomposites. In a typical procedure, 1.88 g of poly(vinyl pyrrolidone) (PVP, Aldrich, Mw = 30,000 g·mol^{-1}) was added in 8.0 mL of deionized water, and the mixture was heated to 60 °C in air under magnetic stirring until PVP was dissolved completely. Then, 1.5 mmol $BiFeO_3$ was added to the PVP solution which was stirred for 20 min. After that, 3 mL

$AgNO_3$ solution was immediately poured to obtain a proper Ag: $BiFeO_3$ ratio. The reaction was carried out for 2 h at 80 °C under magnetic stirring. The product was collected by centrifugation and washed with deionized water. The samples were dried for further use. When the molar ratio between $BiFeO_3$ and $AgNO_3$ was varied from 50, through 30 and 15 to 10, the samples prepared marked with Ag-BFO-1, Ag-BFO-2, Ag-BFO-3, Ag-BFO-4, respectively.

The N-doped TiO_2(N-TiO_2) reference photocatalyst was prepared by the nitridation of commercially available TiO_2 powder (surface area 48 m^2 g^{-1}) at 500 °C for 10 h under NH3 flow (flow rate of 350 mL min^{-1}).

2.3 Photocatalytic activity measurement

The photocatalytic activity of Ag/$BiFeO_3$ nanomaterials was evaluated by the degradation of MO in aqueous solution under visible light irradiation with a 450 W Xe lamp (Newport Solar Simulators, Model: 9115X, a cutoff filter of 420 nm). In each experiment, 50 mL of MO (20 mg/L) solution was added to a glass flask containing 50 mg photocatalyst. The glass flask was in the dark for half an hour to ensure that adsorption equilibrium was reached before the measurements. The reaction temperature was kept at room temperature by cooling water for eliminating any thermal catalytic effect. After the degradation of a period of time, the suspensions containing the sample powders and dyes were sampled. The sample powders were then separated by centrifuging, and the absorbance of the dye solutions was measured using a UV–Vis spectrophotometer. The MO concentration was determined according to absorbance and a standard curve.

2.4 Characterization

The crystal structures of products were characterized by PANalytical X'Pert PRO X-ray diffraction (XRD) with Cu Kα radiation ($\lambda = 1.54$ Å) in the range of 10°–80°. The micrographs of Ag/$BiFeO_3$ composites were investigated using a scanning electron microscope (SEM) and transmission electron microscope (TEM).

3 Results and discussion

3.1 Component analysis of $BiFeO_3$ particle and Ag/$BiFeO_3$ nanocomposites

The phase composition and structure of the samples prepared under different conditions were examined by powder X-ray diffraction (XRD). Figure 1 shows the XRD patterns of the prepared $BiFeO_3$ samples at different temperatures. All diffraction peaks of the sample prepared at 550 °C (Fig. 1b)

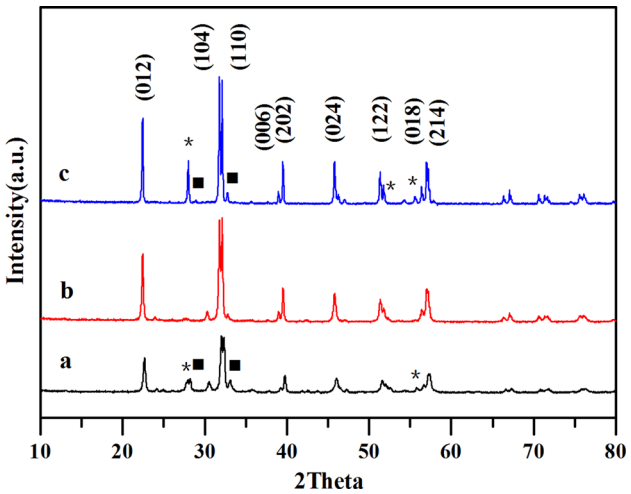

Fig. 1 The XRD patterns of nano-$BiFeO_3$ prepared at different temperatures: *a* 450 °C; *b* 550 °C; *c* 600 °C

are in excellent accord with JPCDS files No. 86-1518. This indicated single-phase $BiFeO_3$ was completely crystallized into the perovskite phase at 550 °C with lattice constants $a = b = 0.5576$ and $c = 0.13866$ nm. From Fig. 1c, we observed the enhanced diffraction peaks of $BiFeO_3$ samples except for a small amount of miscellaneous peak. As increasing the calcination temperature to 600 °C (Fig. 1c), the crystallization of the sample slightly increased. The high heating temperature induced the formation of the impurity Bi_2O_3 and $Bi_{25}FeO_{40}$, which was marked with "asterisk" and "filled square box," respectively. According to the literature, the high heating temperature tends to induce the formation of the impurity when synthesizing of $BiFeO_3$ by sol–gel technique [13]. Furthermore, the lower heating temperature would also induce impurity such as Bi_2O_3 [27]. Figure 1a is the XRD pattern of sample calcined at 400 °C. From this curve, we can also observe the trace amount of Bi_2O_3 and $Bi_{25}FeO_{40}$ with characteristic 2θ values. These results indicate we should choose a proper calcination temperature for obtaining pure phase $BiFeO_3$, which is preferably 550 °C in this method.

3.2 Topography characterization of Ag/$BiFeO_3$ nanocomposites

Figure 2 exhibits the XRD patterns of Ag/$BiFeO_3$ hybrid materials. From curve b to d in Fig. 2, we can see the four diffraction peaks at 38.1, 44.3, 64.2 and 77.5° which are, respectively, corresponding to the (111), (200), (220) and (311) crystalline planes of metallic Ag and are marked with "inverted filled triangle." The positions of the four peaks are perfectly matched with cubic phase Ag (metallic Ag, JCPDS file: 65-2871). Moreover, the intensity of the four diffraction peaks increases with the growth of $AgNO_3$ dosage. The curve a is the XRD pattern of pure phase

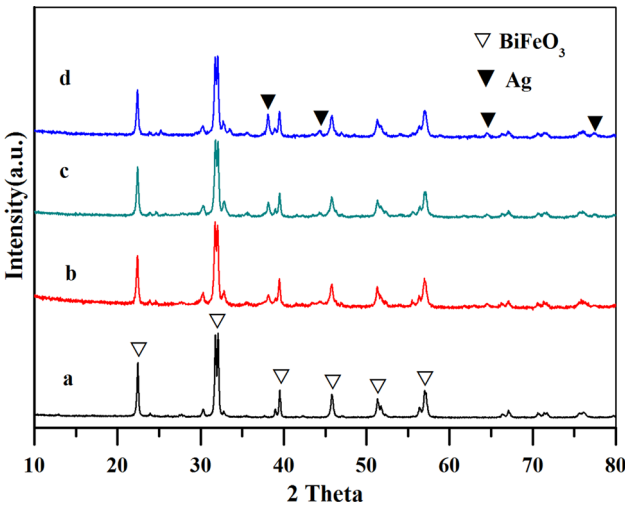

Fig. 2 The XRD patterns of *a* $BiFeO_3$ nanoparticles, *b* Ag-BFO-1, *c* Ag-BFO-2 and *d* Ag-BFO-3. $BiFeO_3$ nanoparticles were prepared at 550 °C

$BiFeO_3$ which was prepared at the temperature of 550 °C. The diffraction peaks of BFO marked with "inverted open triangle." These results illustrate the formation of metallic Ag and $BiFeO_3$ composites and the content of metallic Ag in composites increasing with the growth of $AgNO_3$ dosage.

The morphology of the Ag/$BiFeO_3$ nanocomposites is exhibited in Fig. 3. The SEM image of the Ag/$BiFeO_3$ nanocomposites (Fig. 3a) shows that the size of $BiFeO_3$ is not very uniform, and the Ag NPs are anchored to its surface. To further confirm the presence of the Ag NPs in Ag/$BiFeO_3$ nanocomposites, we presented the TEM image as shown in Fig. 3b. By closely observing Fig. 3b, we find that many small Ag nanoparticles are dispersed on the surface of $BiFeO_3$, and the nanoparticles are irregular and monodisperse with diameters of about 20–50 nm. These results are in good agreement with the XRD data.

3.3 UV–Vis diffuse reflection spectra of Ag/$BiFeO_3$ nanocomposites

The optical properties of the $BiFeO_3$ nanoparticles and its composites with Ag were investigated by UV–Vis diffuse reflection spectroscopy. As shown in Fig. 4, the visible light absorbance of BFO sharp declines when wavelength is longer than 560 nm (curve a), while the absorption of Ag/$BiFeO_3$ at this region is obviously higher than BFO. This could be attributed to surface plasmon absorption of metallic silver on the $BiFeO_3$ surface. $BiFeO_3$ is decorated with the silver nanoparticles with great many different diameters, so Ag/$BiFeO_3$ nanocomposites have the higher absorption in the entire visible light range.

At the range with wavelength shorter than 560 nm, the absorption of all samples is associated with the optical band gap of $BiFeO_3$. In addition, for the Ag/$BiFeO_3$ composites, the absorbance at the range of 560–800 nm

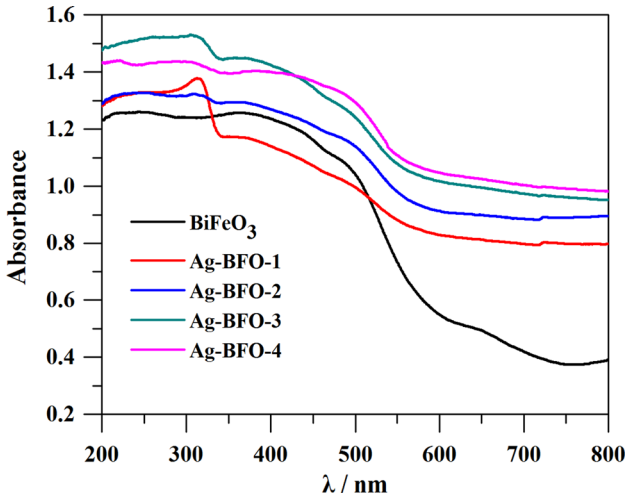

Fig. 4 UV–Vis diffuse reflection spectra of the $BiFeO_3$ nanoparticles and Ag/$BiFeO_3$ nanocomposites

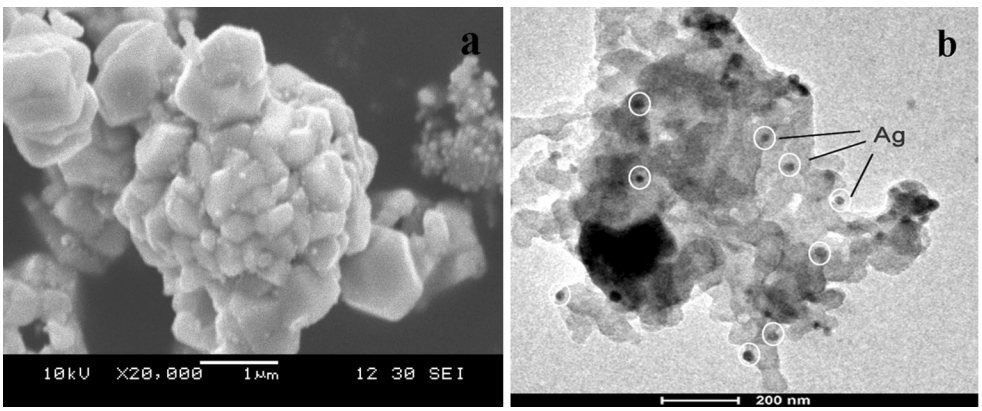

Fig. 3 **a** SEM and **b** TEM images of Ag/$BiFeO_3$ nanocomposites (Ag-BFO-3)

increases in the following order: Ag-BFO-1 ‹ Ag-BFO-2 ‹ Ag-BFO-3 ≈ Ag-BFO-4. These results indicate the absorption intensity of the composites increases with the increasing amount of $AgNO_3$ in reaction system. According to the XRD data, the amount of Ag nanoparticles on the surface of $BiFeO_3$ increases with the growth of amount of silver nitric. Therefore, the increment of the absorbance of composites is due to larger LSPR effect from more Ag nanoparticles deposited on the $BiFeO_3$ surface.

3.4 The photocatalytic performance of Ag/$BiFeO_3$ nanocomposites

Many groups have studied the photocatalytic activities of bismuth ferric nanomaterials by degrading rhodamine B [28], Congo red [12], methylene blue [29] and methyl orange [30] and so on. Results demonstrated $BiFeO_3$ micro/nanocrystals can decompose such kind of dyes under visible light irradiation. The photocatalytic efficiency is dependent on the size, morphology, doping and other modification of BFO.

As a typical organic contaminant, MO is commonly chosen as an organic model compound in wastewater photocatalytic degradation studies. There are two reasons. One is that MO is very stable under visible light irradiation without photocatalyst, and the degradation rate of MO could be ignored after a long-time UV–Vis irradiation in the absence of photocatalyst [30, 31]. The other one is that the amount of absorbed on the catalyst surface could be negligible [32, 33].

Visible light photocatalytic activities of the as-prepared bismuth ferritic nanocrystals were monitored through the degradation of methyl orange in aqueous solution. Figure 5 displays the concentration–time plot of MO photodegradation with BFO nanocrystals obtained at different temperatures as photocatalysts. It is clear that all samples have photocatalytic activity, and the time-dependent change of concentration of MO has a similar trend. The MO degradation rates reach only about 26, 36 and 18 % for BFO nanocrystals synthesized at 450, 550 and 600 °C, respectively, indicating that the photodegradation rate of BFO photocatalysts increases with the increase in temperature from 450 to 550 °C. However, the photocatalytic efficiency of BFO nanoparticles calcined at 600 °C is lower than those of other samples. This could be ascribed to more impurities appeared in BFO nanocrystals at higher or lower temperature. The above comparative results signify that the photodegradation efficiency of BFO nanoparticles is not extremely perfect even for pure phase $BiFeO_3$ nanoparticles compared with that of other visible light photocatalysts containing bismuth element under the same conditions, such as $BiVO_4$ and Bi_2WO_6 [34, 35].

Figure 6 represents the concentration changes of MO as a function of time with various Ag/$BiFeO_3$ photocatalysts under visible light irradiation. For comparison, we also measured the photocatalytic activity of N-TiO_2 in the same condition. Obviously, BFO nanoparticles have much lower photocatalytic activity than the Ag/$BiFeO_3$ composites and N-TiO_2. After 120-min illumination with photocatalyst, the degradation rate of MO was in the following order: BFO nanoparticles <N-TiO_2<Ag-BFO-1<Ag-BFO-2<Ag-BFO-3<Ag-BFO-4, implying that modification with silver nanoparticles can significantly improve the photocatalytic efficiency of BFO, and the activity of the photocatalysts increases further for the more dosage of $AgNO_3$. In addition, MO can be completely decomposed within 90 min under visible light using Ag-BFO-4, which shows that photodegradation performance of Ag-BFO-4 was the best compared with other samples. The kinetic linear simulation curves of photocatalytic degradation of MO with BFO or Ag/$BiFeO_3$ nanocomposites are shown in Fig. 7. The

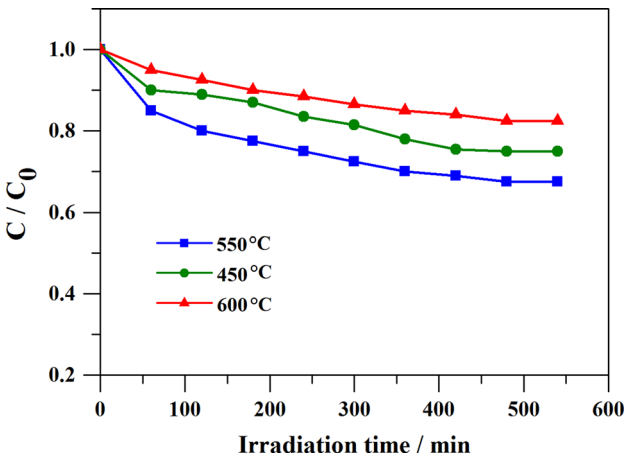

Fig. 5 Photocatalytic degradation of MO as a function of the irradiation time under visible light by the bismuth ferritic nanocrystals prepared at different temperatures

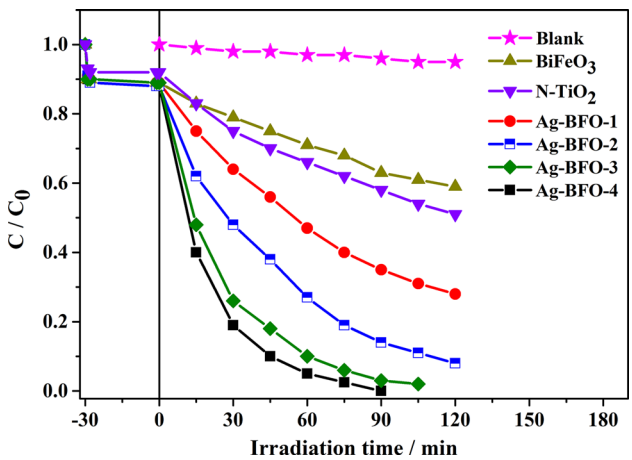

Fig. 6 The photodegradation efficiencies of MO as a function of irradiation time under visible light by samples

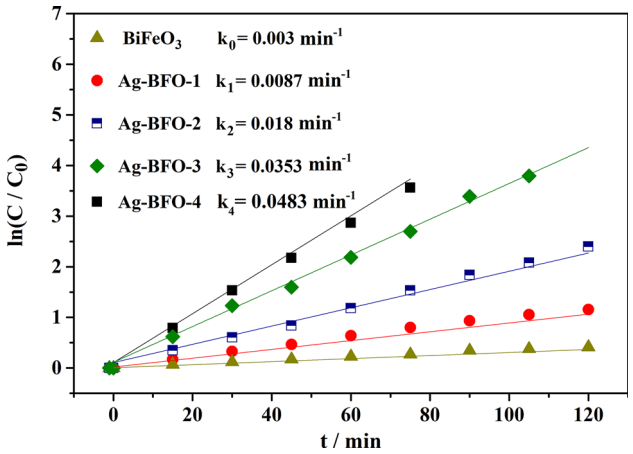

Fig. 7 Kinetic linear simulation curves of photocatalytic degradation of MO with samples

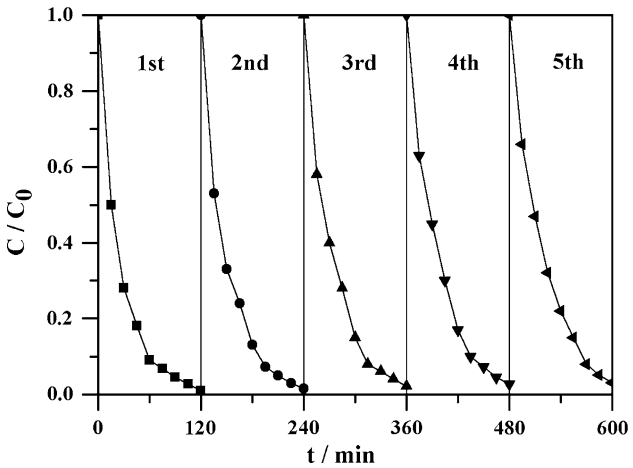

Fig. 8 Recycle experiment of $Ag/BiFeO_3$ (Ag-BFO-3) photocatalyst in the decomposition of MO under visible light irradiation

results show a linear relationship between $\ln(c/c_0)$ (c_0, the initial concentration of MO before irradiation; c, the concentration of MO after irradiation) and irradiation time, which illustrated the photocatalytic decomposition of MO following first-order kinetics. The apparent first-order rate constant k for BFO or $Ag/BiFeO_3$ nanocomposites is 0.003, 0.0087, 0.018, 0.0353, 0.0483 min^{-1}, respectively. Simply, $k(BFO) \ll k(Ag\text{-}BFO\text{-}1) < k(Ag\text{-}BFO\text{-}2) < k(Ag\text{-}BFO\text{-}3) \approx k(Ag\text{-}BFO\text{-}4)$. The results reveal that metal Ag decoration plays an important role for increasing BFO composites photocatalytic activity, but this effect does not enhance further when the molar ratio of $BiFeO_3$ and Ag was less than 18. This indicates that too much Ag NPs on the surface would block the visible light absorption of $BiFeO_3$. Thus, excessive Ag NPs on the surface would not continue to improve the photocatalytic performance of the nanocomposites. In fact, we immersed the catalyst sample in the MO solution in the dark for half an hour to ensure that adsorption equilibrium was reached before the measurements. The MO concentration decreases ~9 % when adsorption equilibrium was reached. And the photolysis of MO was studied by making a measurement under illumination without the catalyst. From Fig. 6, we can see that MO is only photolyzed by about 3 % in the absence of photocatalyst. Thus, the results are really due to photocatalysis instead of adsorption or photolysis which is negligible.

The photocatalytic stability was studied by the cycling degradation experiments. As shown in Fig. 8, although the photocatalytic activity of the as-prepared $Ag/BiFeO_3$ nanocomposites decreases by ~15 % after five times recycle experiment, the activity of $Ag/BiFeO_3$ (Ag-BFO-3) photocatalyst still maintains a high level. The slight decrease after each cycle would be attributed to the absorption of contamination and the decrease in active spots [36].

Fig. 9 Photocatalytic mechanism of $Ag/BiFeO_3$

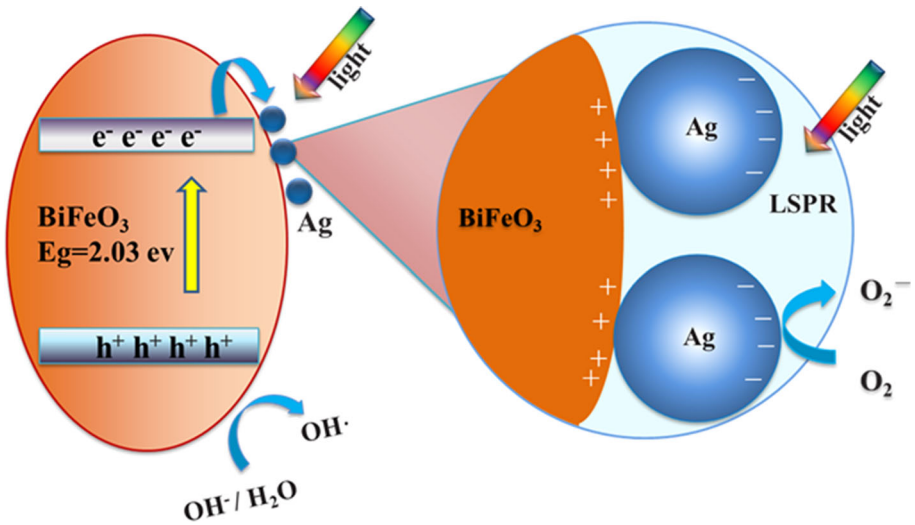

On the basis of the above results, we think the Ag/$BiFeO_3$ nanocomposites can work as a stable and effective visible light photocatalyst applied in the decomposition of organic pollutants.

3.5 The photocatalytic mechanism of Ag/$BiFeO_3$ nanocomposites

Figure 9 illustrates the photocatalytic mechanism of the photoinduced charge separation, migration and degradation process under visible light irradiation. Under visible light illumination, the electrons of $BiFeO_3$ could be excited and then injected into the Fermi level of Ag directly or indirectly. This is due to that the metallic silver nanoparticles can accept the photogenerated electrons from the excited semiconductor as an electron reservoir, thereby facilitating dioxygen reduction by suppressing electron–hole recombination and promoting interfacial charge transfer [36, 37]. Whereas hole is stay in the HOMO of $BiFeO_3$ and oxidizes OH^- and/or H_2O to $OH^{\bullet}$. Furthermore, the localized surface plasmon resonance (LSPR) induced by the collective oscillations of surface electrons on Ag nanoparticles could enhance the visible light harvesting of photocatalyst and help electron–hole separation [38]. As a result, Ag/$BiFeO_3$ had a greater visible absorption ability and a quicker charge separation velocity than $BiFeO_3$ nanocrystals and thus had higher photocatalytic efficiency.

4 Conclusions

In conclusion, Ag/$BiFeO_3$ nanocomposites were successfully synthesized through a sol–gel process, followed by a chemical reduction method. The visible light photoactivities of as-prepared Ag/$BiFeO_3$ photocatalyst were evaluated through the decomposition of MO. The Ag-loaded $BiFeO_3$ nanocomposites showed the higher photocatalytic efficiency compared with the pure BFO particles which could be ascribed to electronic effect of Ag nanoparticles including LSPR and Schottky barrier. Moreover, the photocatalytic activity was found to increase with the further growth of the $AgNO_3$ dosage. We have demonstrated that the photocatalytic performance of $BiFeO_3$ was obviously improved by Ag decoration. The composite photocatalyst retained 85 % activity after five runs, suggesting very good recoverability. Otherwise, Ag/$BiFeO_3$ hybrids have some magnetism (data are not showed in paper), so that the photocatalyst can be conveniently separated from aqueous solution through centrifugation. Therefore, noble metal-loaded $BiFeO_3$ composites with high-efficiency photoactivity and magnetism could promisingly expand the scope of the perovskite ABO_3-structured materials applied in photocatalysis.

Acknowledgments This work was supported by the National Natural Science Foundation of China (51202040, 21363006), Guangxi Natural Science Foundation (2013GXNSFBA019042, 2012GXNSFBA053032) and scientific research projects of Guangxi Education (200103YB059, 201106LX243).

References

1. Song CY, Xu J, Yimamu A, Wang L (2014) Hydrothermal synthesis of perovskite bismuth ferrite micro/nano powders. Integr Ferroelectr 153:33–41
2. Zhu X, Zhou J, Jiang M, Xie J, Liang S, Li S, Liu Z, Zhu Y, Zhu J, Liu Z (2014) Molten salt synthesis of bismuth ferrite nano- and microcrystals and their structural characterization. J Am Ceram Soc 97:2223–2232
3. Ramesh R (2014) Electric field control of ferromagnetism using multi-ferroics: the bismuth ferrite story. Philos Trans R Soc A Math Phys Eng Sci 372:1471–2962
4. Wang J, Neaton JB, Zheng H, Nagarajan V, Ogale SB, Liu B, Viehland D, Vaithyanathan V, Schlom DG, Waghmare UV, Spaldin NA, Rabe KM, Wuttig M, Ramesh R (2003) Epitaxial $BiFeO_3$ multiferroic thin film heterostructures. Science 299:1719–1722
5. Hopkins PE, Adamo C, Ye L, Huey BD, Lee SR, Schlom DG, Ihlefeld JF (2013) Effects of coherent ferroelastic domain walls on the thermal conductivity and Kapitza conductance in bismuth ferrite. Appl Phys Lett 102:121903
6. Seidel J, Martin LW, He Q, Zhan Q, Chu YH, Rother A, Hawkridge ME, Maksymovych P, Yu P, Gajek M, Balke N, Kalinin SV, Gemming S, Wang F, Catalan G, Scott JF, Spaldin NA, Orenstein J, Ramesh R (2009) Conduction at domain walls in oxide multiferroics. Nat Mater 8:229–234
7. Zhang D, Shi P, Wu X, Ren W (2013) Structural and electrical properties of sol–gel-derived Al-doped bismuth ferrite thin films. Ceram Int 39(Supplement 1):S461–S464
8. Bu Y, Zhong Q, Xu D, Tan W (2013) Redox stability and sulfur resistance of Sm0.9Sr0.1CrxFe1−xO3−δ perovskite materials. J Alloys Compd 578:60–66
9. Jeon NJ, Noh JH, Kim YC, Yang WS, Ryu S, Seok SI (2014) Solvent engineering for high-performance inorganic–organic hybrid perovskite solar cells. Nat Mater 13:897–903
10. Armstrong EN, Duncan KL, Wachsman ED (2013) Effect of A and B-site cations on surface exchange coefficient for ABO3 perovskite materials. PCCP 15:2298–2308
11. Ryu S, Noh JH, Jeon NJ, Chan Kim Y, Yang WS, Seo J, Seok SI (2014) Voltage output of efficient perovskite solar cells with high open-circuit voltage and fill factor. Energy Environ Sci 7:2614–2618
12. Li S, Lin Y, Zhang B, Wang Y, Nan C (2010) Controlled fabrication of $BiFeO_3$ uniform microcrystals and their magnetic and photocatalytic behaviors. J Phys Chem C 114:2903–2908
13. Wang X, Lin Y, Ding X, Jiang J (2011) Enhanced visible-light-response photocatalytic activity of bismuth ferrite nanoparticles. J Alloys Compd 509:6585–6588
14. Tan G, Zheng Y, Miao H, Xia A, Ren H (2012) Controllable microwave hydrothermal synthesis of bismuth ferrites and photocatalytic characterization. J Am Ceram Soc 95:280–289
15. Wang W, Li N, Chi Y, Li Y, Yan W, Li X, Shao C (2013) Electrospinning of magnetical bismuth ferrite nanofibers with photocatalytic activity. Ceram Int 39:3511–3518
16. Fei L, Yuan J, Hu Y, Wu C, Wang J, Wang Y (2011) Visible light responsive perovskite $BiFeO_3$ pills and rods with dominant {111}c Facets. Cryst Growth Des 11:1049–1053
17. Tholkappiyan R, Vishista K (2014) Effect of niobium on the optical and magnetic properties of bismuth ferrite ($BiFeO_3$). Adv Sci Eng Med 6:311–317

18. Mukherjee A, Banerjee M, Basu S, Pal M (2014) Electrical and optical properties of gadolinium doped bismuth ferrite nanoparticles. AIP Conf Proc 1591:1339–1341
19. MacLaren I, Wang LQ, Schaffer B, Ramasse QM, Craven AJ, Selbach SM, Spaldin NA, Miao S, Kalantari K, Reaney IM (2013) Nanorods: novel nanorod precipitate formation in neodymium and titanium codoped bismuth ferrite. Adv Funct Mater 23:654
20. Guo R, Fang L, Dong W, Zheng F, Shen M (2010) Enhanced photocatalytic activity and ferromagnetism in Gd doped $BiFeO_3$ nanoparticles. J Phys Chem C 114:21390–21396
21. Zhao G, Liu S, Lu Q, Xu F, Sun H, Yu J (2013) Synthesis of TiO_2/Bi_2WO_6 nanofibers with electrospinning technique for photocatalytic methyl blue degradation. J Sol Gel Sci Technol 66:406–412
22. Talebian N, Nilforoushan M, Memarnezhad P (2013) Photocatalytic activities of multilayered ZnO-based thin films prepared by sol–gel route: effect of SnO_2 heterojunction layer. J Sol Gel Sci Technol 65:178–188
23. Li Z, Shen Y, Yang C, Lei Y, Guan Y, Lin Y, Liu D, Nan C (2013) Significant enhancement in the visible light photocatalytic properties of $BiFeO_3$-graphene nanohybrids. J Mater Chem A 1:823–829
24. Sakar M, Balakumar S, Saravanan P, Jaisankar SN (2013) Manifestation of weak ferromagnetism and photocatalytic activity in bismuth ferrite nanoparticles. AIP Conf Proc 1512: 228–229
25. Kim JK, Kim SS, Kim W-J (2005) Sol–gel synthesis and properties of multiferroic $BiFeO_3$. Mater Lett 59:4006–4009
26. Washio I, Xiong Y, Yin Y, Xia Y (2006) Reduction by the end groups of poly(vinyl pyrrolidone): a new and versatile route to the kinetically controlled synthesis of Ag triangular nanoplates. Adv Mater 18:1745–1749
27. Farhadi S, Rashidi N (2010) Preparation and characterization of pure single-phase BiFeO3 nanoparticles through thermal decomposition of the heteronuclear $Bi[Fe(CN)_6]\cdot 5H_2O$ complex. Polyhedron 29:2959–2965
28. Zhu X, Hang Q, Xing Z, Yang Y, Zhu J, Liu Z, Ming N, Zhou P, Song Y, Li Z, Yu T, Zou Z (2011) Microwave hydrothermal synthesis, structural characterization, and visible-light photocatalytic activities of single-crystalline bismuth ferric nanocrystals. J Am Ceram Soc 94:2688–2693
29. Huo Y, Jin Y, Zhang Y (2010) Citric acid assisted solvothermal synthesis of $BiFeO_3$ microspheres with high visible-light photocatalytic activity. J Mol Catal A Chem 331:15–20
30. Gao F, Chen XY, Yin KB, Dong S, Ren ZF, Yuan F, Yu T, Zou ZG, Liu JM (2007) Visible-light photocatalytic properties of weak magnetic $BiFeO_3$ nanoparticles. Adv Mater 19:2889–2892
31. Romão J, Barata D, Habibovic P, Mul G, Baltrusaitis J (2014) High throughput analysis of photocatalytic water purification. Anal Chem 86:7612–7617
32. Song L, Li Y, Zhang S, Zhang S (2014) Synthesis and characterization of Bi^{3+}-Doped Ag/AgCl and enhanced photocatalytic properties. J Phys Chem C 118:29777–29787
33. Yamada Y, Mizutani M, Nakamura T, Yano K (2010) Mesoporous microcapsules with decorated inner surface: fabrication and photocatalytic activity. Chem Mater 22:1695–1703
34. Yu J, Kudo A (2006) Effects of structural variation on the photocatalytic performance of hydrothermally synthesized $BiVO_4$. Adv Funct Mater 16:2163–2169
35. Fu H, Pan C, Yao W, Zhu Y (2005) Visible-light-induced degradation of rhodamine B by Nanosized Bi_2WO_6. J Phys Chem B 109:22432–22439
36. Yang Y, Wen J, Wei J, Xiong R, Shi J, Pan C (2013) Polypyrrole-decorated Ag–TiO_2 nanofibers exhibiting enhanced photocatalytic activity under visible-light illumination. ACS Appl Mater Interf 5:6201–6207
37. Liu R, Wang P, Wang X, Yu H, Yu J (2012) UV- and visible-light photocatalytic activity of simultaneously deposited and doped Ag/Ag(I)-TiO_2 photocatalyst. J Phys Chem C 116:17721–17728
38. Zhang Z, Wang W, Gao E, Sun S, Zhang L (2012) Photocatalysis coupled with thermal effect induced by SPR on Ag-Loaded Bi_2WO_6 with enhanced photocatalytic activity. J Phys Chem C 116:25898–25903